Liquid-Liquid Microfluidic Flows for Ultrafast 5-hydroxymethyl Furfural Extraction

Tai-Ying Chen, [#,a] Pierre Desir, [#,a] Mauro Bracconi,[c] Basudeb Saha,[b] Matteo Maestri, [c] and Dionisios G. Vlachos [a, b, *]

[a] Department of Chemical and Biomolecular Engineering, University of Delaware, 150 Academy Street, Newark, Delaware 19716, United States

[b] Catalysis Center for Energy Innovation, RAPID Manufacturing Institute, Delaware Energy Institute (DEI), 221 Academy Street, Newark, Delaware 19716, United States

[c] Laboratory of Catalysis and Catalytic Processes, Dipartimento di Energia, Politecnico di Milano, via La Masa 34, 20156 Milano, Italy

[#] These authors contributed equally.

[*] Corresponding author; vlachos@udel.edu (D.G. Vlachos)

Abstract

We study the effects of liquid-liquid flow patterns on the extraction of 5-hydroxymethyl furfural from the aqueous phase into an organic phase (methyl isobutyl ketone, ethyl acetate, and 2-pentanol) at ultrashort residence times of 0.2 – 20 s in a coiled capillary microchannel. Slug, droplet, slug-droplet, dispersed, parallel, annular, and irregular two-phase flow patterns are generated. We evaluate the extraction efficiency and the volumetric mass transfer coefficient via experiments and computational fluid dynamics (CFD). The CFD predictions are in quantitative agreement with the experimental data. The convective and diffusive contribution to the mass transfer of different flow patterns is analyzed. For all solvent pairs, the extraction efficiency varies irregularly with increasing flow rate due to changes in the mass transfer mechanism caused by a transition between flow regimes. Overall, we demonstrate >90% extraction efficiencies with high volumetric mass transfer coefficients ranging from 0.006 to 2.17 s^{-1}. Furthermore, a merit index is defined to assess the tradeoff between the fast mass transfer and the pressure drop in biphasic microchannels. In general, the mass transfer rate increases significantly at high flow rates at the expense of a high-pressure drop. The ethyl acetate/water irregular flow pattern is optimal due to large throughput, extraction efficiency, and mass transfer coefficient, with minimal pressure drop.

Keywords: Biphasic flow, computational fluid dynamics, 5-hydroxymethyl furfural, mass transfer, microreactors

Introduction

Recent developments in microtechnology have showcased the potential of continuous flow microreactors in process intensification. In particular, the small characteristic length scale of a capillary microchannel (~μm) provides heat and mass transfer rates that surpass traditional large-scale batch or continuous flow reactors by orders of magnitude [1-5]. Hence, in reactions with by-products, microreactors can enable operation with significant improvement in product yield and reactor throughput by suppressing by-product formation and reducing reaction times from hours down to milliseconds [5-9]. Liquid-liquid biphasic microreactors have extensively been used for the extraction of unstable intermediates formed in the aqueous phase into an immiscible organic phase preventing further product degradation [10-18]. For these systems, the interfacial tension between two phases gives way to a wide variety of flow patterns [17-22] with high interfacial area enabling the fast mass transfer of solute. The generated flow patterns include stable flows with a uniform and tunable interfacial area (slug and droplet flow), stable flows with a fixed interfacial area (parallel and annular flow), and unstable transitional flows with irregular and unsteady interfacial area (slug-droplet, pearl necklace, dispersed, deformed interface, and irregular flow) [23-25].

An exciting application of liquid-liquid microreactor technology is lignocellulosic biomass conversion to renewable fuels, lubricants, and other bio-materials. In particular, the cellulose-based C_6 sugars, glucose and fructose, can undergo acid-catalyzed dehydration in water to 5-hydroxymethylfurfural (HMF) [26-29]. HMF production suffers from low selectivity resulting from by-product formation, namely HMF rehydration to levulinic acid and formic acid and polymeric humins [30-32]. While biphasic batch reactors obtain higher yields of HMF by reactive extraction [33-36], the use of large volumes of organic solvents has limited their application [27, 37]. High throughput and scalable HMF production need elevated temperatures and short contact times that escape batch reactors due to slow heat and mass transfer [38]. Liquid-liquid biphasic microreactors were introduced for HMF production [37, 39-43] but focused on slug flow [37, 39, 40, 43] or dripping flow [42], at reaction times spanning from 40 s to 12 min [39, 40].

The effect of the flow patterns has been studied in other systems [4, 16, 17, 21, 23]. For example, Dessimoz *et al.* [21] have studied the extraction of CCl_3COOH in slug and parallel flows of toluene/water and hexane/water systems. The volumetric mass transfer coefficients for both slug and parallel flow, 0.2 - 0.5 s^{-1}, are comparable and one order of magnitude greater than the conventional spray column and impinging streams [21]. Moreover, Jovanovic *et al.* [16] have observed that bubble and slug flow result in 100% extraction of 2-butanol in a toluene/water microreactor and are stable. In contrast, the extraction of annular and parallel flows is 47% and 30%, respectively, and the flows are unstable as the capillary length increased. Consequently, there is a lack of understanding of flow patterns' effects on the reactive extraction for HMF production at short residence times. Furthermore, very few works have investigated the mass transfer characteristics of biphasic microreactors for HMF extraction [37, 42], which is necessary to determine the operation window to prevent or minimize mass transfer limitations at elevated temperatures and short residence times.

An accurate simulation method of multiphase mass transport can help understand the mass transfer characteristics by reducing the number of experimental measurements and providing detailed transient velocity and concentration fields. Haroun *et al.* [44] have initially developed a continuous species transfer (CST) method to model the species mass transport across the interface between two phases. Marschall *et al.* [45] have improved the model aiming at the simulation of three dimensional and complex geometries. Later, Deising *et al.* [46] generalized the methodology to fully

2

resolve the mass transfer between phases characterized by a sharp transition in the species concentration across the interface [47]. Nieves-Remacha et al. [48] have applied this method to investigate the scale-up of a flow reactor. Moreover, Yang et al. [49] characterized segmented flow microreactors with the CST and revealed the potential numerical error of the CST method at high local, i.e., cell-based, Péclet numbers. More recently, Maes and Soulaine [50, 51] improved the methodology by introducing a new compressive scheme, which can avoid the sizeable numerical diffusion generated by the standard CST method. They simulated interfacial species transfer in a complex porous medium at low Capillary numbers with high accuracy, overcoming the conventional method's limitation.

Building on these state-of-the-art methods, we aim at applying a combined experimental and computational approach to elucidate the effects of the organic/aqueous biphasic flow patterns in a microchannel on the HMF extraction at ultrashort residence times. Methyl isobutyl ketone (MIBK), ethyl acetate (EtAc), and 2-pentanol (2-pentOH), are used as the extracting phase. The two-phase flow patterns in these solvents have previously been investigated [25]. Herein, we experimentally quantify the mass transfer of the biphasic flow patterns during the extraction of HMF. We further employ a 3D computational fluid dynamics (CFD) model to investigate the extraction of different flow patterns and the mass transport mechanism. Finally, we develop metrics to determine the best solvent pair and flow patterns for the HMF extraction under high reactor throughput.

Methods

Experimental methods

Two syringe pumps (New Era PumpSystemsInc. NE-300) or two Waters 515 High-Pressure Liquid Chromatography (HPLC) pumps (Waters Alliance) were used to pump the aqueous and organic solvent feeds into a 500 μm square cross-section T-junction (Valco Instruments) made of polyether ether ketone (PEEK), as seen in Scheme 1. The feed streams come in contact in a opposed-flow configuration at the T-junction to generate the biphasic flow patterns. The biphasic mixture then enters a capillary microchannel made of perfluoroalkoxy alkane (PFA) (Idex Health) with 17 cm of coiled tubing with a circular cross-section with ID = 500 μm and OD = 1600 μm. Deionized water (Milli-Q) was used as the aqueous solvent. EtAc 99% (Sigma Aldrich), MIBK 99% (Sigma Aldrich), and 2-pentOH 99% (Sigma Aldrich) were used as the organic solvents. Sodium fluorescein 99% (Sigma Aldrich) and 9,10-diphenyl anthracene 99% (Sigma Aldrich) were used as the aqueous fluorescent dye and the organic fluorescent dye, respectively, to contrast the two liquid phases during flow visualization.

The biphasic flow patterns were characterized using laser induced fluorescence (LIF) of a 250 μM solution of sodium fluorescein in water and a 10 mM of 9,10-diphenyl anthracene solution in one of the selected organic solvents, using a high-speed confocal microscope (Highspeed LSM 5 Live Duo) mounted with an inverter. Two laser sources with a wavelength of 488 nm and 405 nm were used for the fluorescence excitation of the aqueous and organic solvents, respectively. Images were captured using a Zeiss 1.25X and a 2.5X Plan-Neofluar objective lens at frame rates ranging from 30 to 108.1 fps. Further image analysis and processing of the flow patterns were conducted in ImageJ.

Mass transfer experiments were conducted at room temperature and for various flow conditions. Typically, an aqueous feed of 0.1 wt% HMF in water comes in contact with a neat

3

organic solvent feed at the T-junction where the two-phase flow patterns are generated. As the biphasic mixture flows and HMF is extracted from the aqueous to the organic phase, the exit stream is collected in a 10 mL graduated cylinder placed directly below the outlet of the microchannel. As the two phases settle, immediate and complete phase separation is observed for the solvent pairs used in this study. Using a 2 mL plastic pipette, the top organic phase is quickly removed from the graduated cylinder. Then small aliquots of the aqueous phase are pipetted into 300 µL vials for post-extraction analysis. The extent of mass transfer in the sampling zone is evaluated using the procedure reported by Zhao *et al.*[52] Using the highest flow rate of 10 mL/min considered in the experimental studies and a short microchannel length of 2 cm, we evaluated the extraction efficiency (E) at 4 different sample collection times for the biphasic mixtures used, as shown in the Supporting Information (SI). The extraction efficiency measures the distance from the thermodynamic equilibrium. An E value of 0 indicates no solute extraction (far from phase equilibrium) and 1 implies the maximum extracted HMF (equilibrium). The extraction efficiency is estimated from the HMF concentration:

$$E = \frac{C_{org}^{OUT} - C_{org}^{IN}}{C_{org}^{eq} - C_{org}^{IN}} \tag{1}$$

Here, C_{org}^{IN}, C_{org}^{OUT}, and C_{org}^{eq} are the HMF concentration in the organic phase at the inlet, at the outlet, and at equilibrium, respectively. The method of quantifying the HMF concentration in each phase is discussed in a later section. We performed triplicates of the experiments and calculated the standard deviation in the extraction efficiency. For all the solvent pairs, the extraction efficiency remains unchanged with sampling times ranging from 6 s to 50 s. Furthermore, the standard deviation in E (%) is no more than 4.8%, suggesting that mass transfer in the sampling zone is minimal and the "time extrapolation" method is not required to estimate the extraction efficiency in the microchannel. Table 1 reports the solvent properties for the biphasic systems of this study. The selected solvents are commonly used for HMF extraction and in biomass-derived carbohydrates' conversion. Besides, the interfacial tension, viscosity, and diffusivity of the selected solvents are order of magnitude different to cover a large parameter space. The partition coefficient of HMF was determined for each biphasic system by mixing 3 mL of a 0.1 wt% HMF aqueous solution with 3 mL of the organic solvent in a 15 mL scintillation vial at a stirring rate of 500 rpm for 3 hours to reach equilibrium. The pressure drop across the microchannel was monitored and measured by placing a pressure sensor (Idex Health) at the channel's inlet.

4
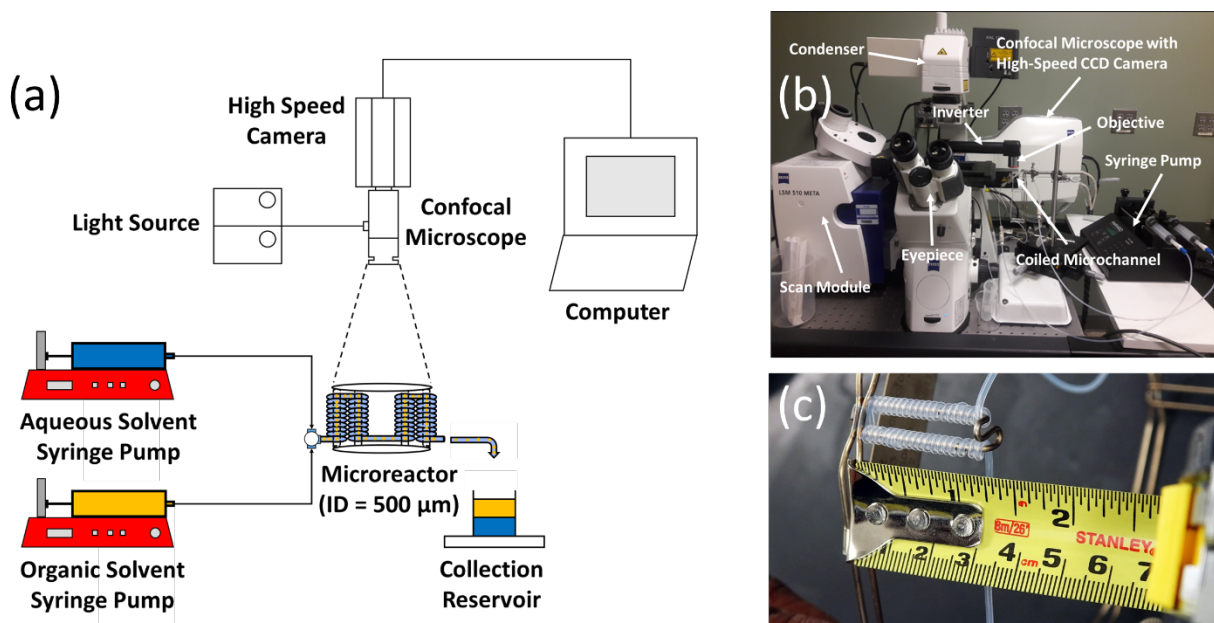
Scheme 1. Schematic diagram of the experimental setup used for (a) flow visualization of the two-phase flow patterns, (b) photograph of the high-speed confocal microscope setup (b), and (c) zoom-in view of the coiled microchannel. Reprinted with permission from Desir et al. [25] Copyright (2020) Royal society of chemistry.

Table 1. Solvent properties of the liquid-liquid mixtures at 20 °C.

Solvent	Kinematic viscosity [m^2/s]	Density [kg/m^3]	Interfacial tension [N/m]	Partition coefficient [-]	Diffusivity[53] [m^2/s]
EtAc	4.90×10^{-7}	900	0.0074	1.4 ± 0.05	2.87×10^{-9}
2-pentOH	4.27×10^{-6}	812	0.0034	1.3 ± 0.07	3.81×10^{-10}
MIBK	7.29×10^{-7}	802	0.0157	1.1 ± 0.03	2.43×10^{-9}
Water	1.00×10^{-6}	998	N.A.	N.A.	1.00×10^{-9}

Computational methods

Two-phase flow CFD simulations are carried out using a Volume-Of-Fluid (VOF) method, which tracks and resolves sharp interfaces between phases. In the VOF method, we employ a single-field approach where the physical properties are calculated as weighted averages based on each phase's content in the computational cells [54], as shown in Eq. (2)

$$\beta = \alpha\beta_1 + (1 - \alpha)\beta_2 \tag{2}$$

5

The interface is located from an indicator function, which is equal to the volume fraction of a phase in each cell, named volume fraction (α). The solution of the continuity equation, Eq. (3), for the volume fraction (α) enables capturing the motion and evolution of the interphase surface [55]

$$\frac{\partial \alpha}{\partial t} + \nabla \cdot (\alpha \mathbf{U}) = 0 \tag{3}$$

where α is the volume fraction and $\mathbf{U}$ is the fluid velocity.

The volume fraction at the interface is discontinuous, resulting in numerical difficulties. To ensure the interphase's sharpness, an additional advection term is introduced [56], as in Eq. (4), which has non-zero values only at the interface, aiming at counterbalancing the numerical diffusion across the interface

$$\frac{\partial \alpha}{\partial t} + \nabla \cdot (\alpha \mathbf{U}) + \nabla \cdot (\alpha(1 - \alpha)\mathbf{U_r}) = 0 \tag{4}$$

where $\mathbf{U_r}$ is the relative velocity between two phases. This term is the compressive velocity normal to the interface and is proportional to the maximum velocity of the field [57], as in Eq. (5)

$$\mathbf{U_r} = \mathbf{n_f} \cdot \min\left[\frac{C_\gamma |\varphi|}{|S_f|}, \max\left(\frac{|\varphi|}{|S_f|}\right)\right] \tag{5}$$

where φ is the volumetric flux at the cell faces, n_f represents a vector normal to the computational cell faces, S_f denotes the cell face area, and C_γ is the compression factor. In this study, we employed a C_γ equal to 1. It is worth emphasizing this equation is exact since its derivation does not involve any additional assumption. A set of single-field equations describes the fluid dynamics of two-phase flows obtained by conditional volume-averaging of the local mass and momentum conservation equations. The single-field conservation equations of mass and momentum are Eqs. (6) and (7)

$$\nabla(\mathbf{U}) = 0 \tag{6}$$

$$\frac{\partial(\rho\mathbf{U})}{\partial t} + \nabla \cdot (\rho\mathbf{U}\otimes\mathbf{U}) = \mu\nabla^2\mathbf{U} - \nabla P + \rho\mathbf{g} + \mathbf{F_{st}} \tag{7}$$

where ρ is the density, μ is the viscosity, P is the pressure and $\mathbf{F_{st}}$ is the surface tension force, which acts only at the interface. All the variables are averaged with respect to the volume fractions, according to Eq. (2).

The surface tension force is introduced into the finite-volume approach using a three-dimensional body force. The continuous surface force (CSF) formulation [58], Eq. (8), is generally employed in VOF simulations

$$\mathbf{F_{st}} = \sigma\kappa\nabla\alpha \tag{8}$$

where σ denotes the surface tension and κ is the curvature. Brackbill *et al.* [58] indicated that the curvature of an interface described by a volume fraction could be computed by taking the divergence of a normal field, $\kappa = \nabla \cdot \mathbf{n}$, in which the normal field is computed from the volume fraction, as in Eq. (9)

$$\mathbf{n} = \frac{\nabla\alpha}{|\nabla\alpha|} \tag{9}$$

6

However, in the CSF approach, the errors of calculating curvature and the normal vector propagate and induce spurious currents at the interface [59]. To mitigate this problem, a sharp surface force (SSF) method is considered [60, 61]. The SSF method introduces a Laplacian smoother to smooth the indicator function and computes the curvature on a curtail function to sharpen the interface [60, 61] as in Eqs. (10) to (12)

$$\mathbf{F_{st}} = \sigma\left(\nabla \cdot \frac{\nabla\widehat{\alpha}}{|\nabla\widehat{\alpha}|}\right)\nabla\widetilde{\alpha} \tag{10}$$

$$\widehat{\alpha} = \frac{\sum \alpha_f S_f}{\sum S_f} \tag{11}$$

$$\widetilde{\alpha} = \frac{\min\left(\max\left(\alpha,\frac{C_s}{2}\right),1-\frac{C_s}{2}\right)-\frac{C_s}{2}}{1-C_s} \tag{12}$$

where α_f is the value of α at the center of faces of each cell and C_s represents a sharpness constant equal to 0.4 in this work, which is suggested by Maes and Soulaine[50]. Here, we employ this smoother two times that it is usually sufficient to achieve a significant reduction of the spurious current [62]. At the liquid/liquid/solid triple point near the walls, the adhesion force needs treatment using a fixed contact angle [58]. The unit-normal vector (**n**) is calculated at the walls as a function of the contact angle as in Eq. (13)

$$\mathbf{n} = \mathbf{n_w}\cos\theta_0 + \mathbf{t_w}\sin\theta_0 \tag{13}$$

where θ_0 is the contact angle, and $\mathbf{n_w}$ and $\mathbf{t_w}$ are the unit normal and tangential vectors to the wall surface. Hence, the value of contact angle defines the wettability. When θ_0 is larger than 90°, wetting of the surface is unfavorable, i.e., the wall is hydrophobic. On the other hand, when θ_0 is smaller than 90°, the fluid spreads over the wall, i.e., the wall is hydrophilic.

The CST model [44, 45] is applied to account for the mass transfer between phases. A species transport equation for species j is formulated, Eq. (14), and considered along with the fluid dynamics equations. Detailed derivations are in the SI. This approach introduces single-field representation and considers the concentration difference in two phases at the interface with an additional discontinuity term Φ, Eq. (15)

$$\frac{\partial C_j}{\partial t} + \nabla \cdot \left(C_j \mathbf{U}\right) = \nabla \cdot \left(\widehat{D}_J \nabla C_j + \Phi_j\right) \tag{14}$$

$$\Phi_j = -\left(\frac{\widehat{D}_J(1-pc)}{\alpha + K(1-\alpha)}\right)C_j\nabla\alpha \tag{15}$$

where C is the single-field concentration; $\widehat{D}_j$ is the harmonic interpolation of the diffusivity of species j in the two phases, as Eq. (16); and K represents the partition coefficient, as Eq. (17)

$$\widehat{D}_J = \frac{1}{\frac{\alpha}{D_{j,1}} + \frac{1-\alpha}{D_{j,2}}} \tag{16}$$

$$K = \frac{C_{j,2}}{C_{j,1}} \tag{17}$$

7

This CST approach works well in the diffusion dominated regime (local Péclet number below 0.5) but requires an extremely refined mesh across the interface when the fluid velocity increases and leads to the inadequate description of the concentration jump and the mass transfer across the interface in the convection dominated regime [49]. To overcome this issue, a compressive continuous species transfer (C-CST) method, which can avoid substantial artificial mass transfer at the interface, has been introduced [50, 51]. The model considers an additional compressive term into the single-field advection flux $\mathbf{F}_j$, i.e., the second term on the left-hand side of Eq. (14), as reported in Eq. (18), in analogy with the compressive term in the volume fraction of the continuity equation

$$\mathbf{F}_j = C_j\mathbf{U} + (C_{j,1} - C_{j,2})\alpha(1 - \alpha)\mathbf{U}_r \tag{18}$$

The newly formulated flux $\mathbf{F}_j$ consists of two terms. The first is equivalent to the original CST formulation, whereas the second is the additional compressive term of non-zero value only at the interface. This additional term mitigates the artificial mass transfer in the convection dominated regime and preserves the sharp interface. It is derived without assumptions and is fully consistent with the phase-tracking Eq. (4) [50]. By combining the partition coefficient and the single-field formulation, the concentration equation with the new advection flux is as Eq. (19)

$$\frac{\partial C_j}{\partial t} + \nabla \cdot (C_j\mathbf{U}) = -\nabla \cdot \left(\frac{(1-K)C_j}{\alpha+K(1-\alpha)}\alpha(1 - \alpha)\mathbf{U}_r\right) + \nabla \cdot (\widehat{D}_j\nabla C_j + \Phi_j) \tag{19}$$

Moreover, the boundary condition for global species concentration at the liquid/liquid/solid triple points [63] is Eq. (20)

$$(\widehat{D}_j\nabla C_j + \Phi_j) \cdot \mathbf{n}_s = 0 \tag{20}$$

These governing equations are implemented and solved using OpenFOAM [64], a finite-volume based, open-source CFD toolbox. A 3D T-shape micromixer with square channels with a size of 0.5 mm is established as the simulation domain in Scheme 2, which shares the same geometric parameters with our experimental system. 5,696,000 cells within the hexahedral simulation domain are employed. In particular, the cell size at the channel's wall is half of that in the middle of the channel. The results are independent of the discretization; additional information is provided in the SI. A maximum Courant number of 0.25 guarantees the stability of the simulation. The simulation setup is as follows. The water contains HMF and flows into the T-mixer from one inlet, while the organic phase, without any HMF, flows into the T-mixer from the other side. The inlet HMF concentration is 0.1 wt% in the aqueous phase and 0% in the organic phase. No-slip condition for velocity and zero gradient for pressure are implemented at the wall of the microchannel. The water contact angle is 180°, and Eq. (20) is applied as the boundary condition at the microchannel wall for the species concentration. At the inlet, a fixed velocity value and zero gradient for the pressure are imposed. At the outlet, the velocity, concentration, and volume fraction are set to be zero gradient, and the pressure to be atmospheric.

8
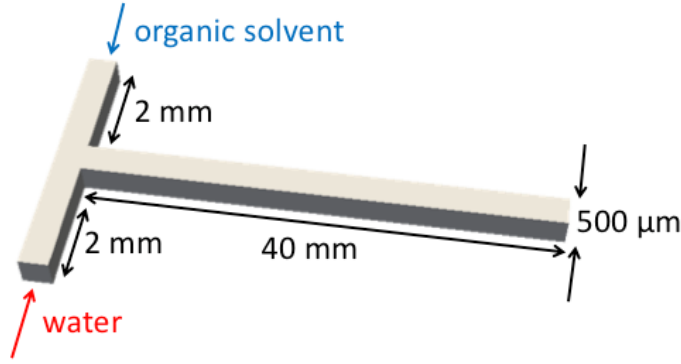
Scheme 2. Flow configuration of the organic and aqueous feeds into the T-junction used for both flow visualization experiments and CFD simulations. The dimensions are indicated.

Mass transfer quantification

The volumetric mass transfer coefficient ($k_L a$), which quantifies the volumetric mass transfer rate between phases during the extraction, is the product of the global mass transfer coefficient (k_L) times the specific interfacial area for mass transfer (a). By considering the mass transfer resistance being in the organic phase and assuming that the coiled microchannel behaves as an ideal plug flow reactor, $k_L a$ under low HMF concentrations is estimated from the mass balances [65]

$$C_{aq}^{IN}\varepsilon_{aq} = C_{aq}\varepsilon_{aq} + C_{org}\varepsilon_{org} \tag{21}$$

$$C_{aq}^{IN}\varepsilon_{aq} = C_{aq}^{eq}\varepsilon_{aq} + C_{org}^{eq}\varepsilon_{org} \tag{22}$$

$$\varepsilon_{aq}\frac{dC_{aq}}{dt} = -k_L a\left(KC_{aq} - C_{org}\right) \tag{23}$$

$$\varepsilon_{org}\frac{dC_{org}}{dt} = k_L a\left(KC_{aq} - C_{org}\right) \tag{24}$$

$$k_L a = \frac{1}{\tau\left[\frac{K}{\varepsilon_{aq}}+\frac{1}{\varepsilon_{org}}\right]}\ln\left(\frac{C_{org}^{eq}-C_{org}^{IN}}{C_{org}^{eq}-C_{org}^{OUT}}\right) \tag{25}$$

where C_{aq}^{IN}, C_{org}^{IN}, C_{aq}, C_{org} are the HMF concentration in the aqueous and organic phase at the inlet, the aqueous and organic phase HMF concentration, respectively, ε_{aq} is the volume fraction of the aqueous solvent, ε_{org} is the volume fraction of the organic solvent, C_{aq}^{eq} is the HMF equilibrium concentration in the aqueous phase, and τ is the mean residence time of the biphasic mixture in the microchannel.

In the experiments, the aqueous and organic HMF concentrations are quantified using HPLC (Water Alliance Instruments). Aqueous aliquots were analyzed post-extraction and HMF was detected and quantified by an Agilent Zorbax SB-C18 heated to 50 °C, using a 50/50 (v/v) acetonitrile and water mixture flowing at 0.3 mL/min as the mobile phase. The HMF concentration in the organic phase was estimated from the mass balance. HMF, 2-pentanol, EtAc, and MIBK eluted at 8.8, 13.7, 13.9, and 19.6 min, respectively. In the simulation, the outlet concentration of

9

HMF in the organic phase is calculated by volume-averaging the concentration within the organic phase.

Results and Discussion

Liquid-liquid flow patterns

The two-phase flow patterns generated in the microchannel with EtAc, MIBK, and 2-pentOH have been previously studied [25]. The flow patterns observed experimentally are summarized in the SI. In total, seven flow regimes are obtained: slug flow, droplet flow, dispersed flow, slug-droplet flow, parallel flow, annular flow, and irregular flow. Generally, the slug flow is the more frequently encountered flow regime at low flow rates (<1 mL/min) over the range of org/aq (v/v) ratios studied (0.25–4) [25]. The droplet flow is generated in a very narrow operation window at intermediate flow rates (~1 mL/min) [25], and the dispersed flow is usually obtained at high flow rates (>1 mL/min) and low org/aq (v/v) ratios [25].

Experimental mass transfer in biphasic systems

Mass transfer studies were conducted in the coiled microchannel for residence times of 0.2–20 s.. Figure 1 plots the estimated $k_L a$ vs. the total volumetric flow rate (Q_{total}) and the mean residence time, for all the flow patterns observed with three organic solvents at different org/aq (v/v) ratios. The reported error bars represent the standard deviation from replica experiments. For all the solvent pairs, the volumetric mass transfer coefficient increases with increasing total flow rate or decreasing residence time, except for 2-pentOH, where $k_L a$ changes non-monotonically between $1 - 5$ mL/min. This non-monotonicity is due to the transition from flow dominated by surface forces (slug flow) and strong shear forces (droplet and slug-droplet flow) to flow with high inertia (dispersed, parallel, and annular flow). The changes in the $k_L a$ can be explained by the changes in the mass transport mechanism. For example, the fast solute extraction in a slug or a droplet flow results from the advection by the recirculating motion of Taylor vortices [49]. In contrast, the annular flow under high flow rates suffers from low extraction due to radial molecular diffusion from the aqueous phase to the two confining organic layers. Moreover, the small specific surface area of an annular flow compared to a slug or a droplet flow also contributes to low solute extraction. Interestingly, the transition from the droplet flow to the annular flow, occurring at org/aq (v/v) = 1 for EtAc, shows a continuous increase in $k_L a$, in contrast to the decrease in 2-pentanol. Our flow visualization experiments have shown that the interface of the annular flow formed by EtAc is unstable and this flow pattern breaks down into a slug-droplet flow at longer microchannel lengths while 2-pentanol produces a stable annular flow regime. It follows that the interfacial instabilities in the annular flow regime with EtAc enhance the mass transfer rate by creating additional advection along the radial direction of the microchannel, increasing the volumetric mass transfer coefficient. Under the flow conditions investigated in Figure 1, the highest $k_L a$ values estimated are 0.91, 1.27, and 2.17 s^{-1} for a 2-pentanol/water annular flow, an EtAc/water irregular flow, and a MIBK/water irregular flow, respectively, at $Q_{total} = 10$ mL/min, $\tau = 0.2$ s, and org/aq (v/v) = 1.

Since the organic solvents investigated have low HMF partition coefficients (~1), larger fractions of the organic phase are usually needed to extract HMF. Figure 2 demonstrates the effects of the org/aq (v/v) ratio on the volumetric mass transfer coefficient at fixed flow rates. Non-

10

monotonic variations in $k_L a$ values are also observed when increasing the org/aq (v/v) ratio. This is also likely due to changes in the dominant mass transport mechanism during the transition from one flow regime to another or within the same flow regime. Besides, in Figure 2, a high org/aq (v/v) ratio does not necessarily lead to a high $k_L a$, though more organic solvent likely extracts higher amounts of HMF. This is attributed to the mass transfer rate being mainly dependent on the solvents' physical properties and the flow regimes, but not the amount of the organic solvent. Overall, the $k_L a$ values are in the range of $0.009 - 0.912$ s^{-1}, $0.006 - 1.33$ s^{-1}, and $0.016 - 2.17$ s^{-1} for 2-pentOH, EtAc, and MIBK, respectively. These obtained $k_L a$ values are at the higher end compared to previously reported values (mostly between 0.01 to 3 s^{-1} for channels of similar size) in the literature [7, 12-15, 21]. Furthermore, these $k_L a$ values are orders of magnitude greater than traditional liquid-liquid contactors [14, 27]. To further understand the transport mechanism of different flow patterns, we utilize CFD simulations, as discussed below.
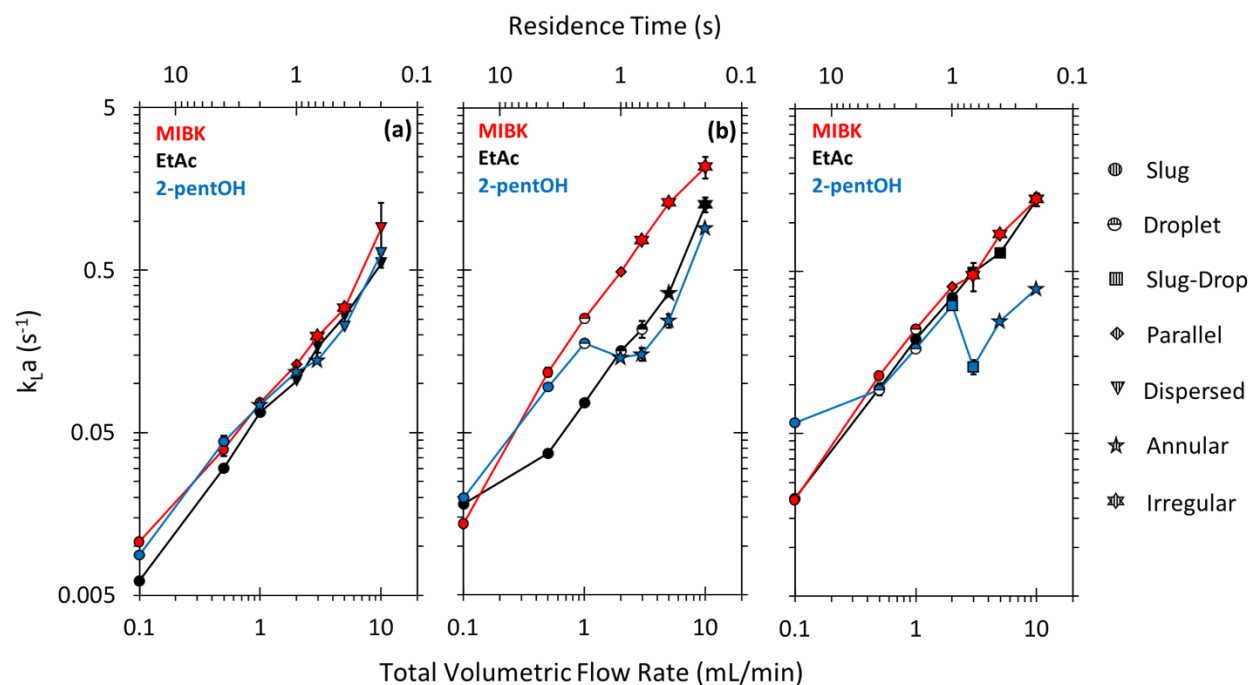

Figure 1. Volumetric mass transfer coefficient obtained from experiments as a function of the total volumetric flow rate and the mean residence time in the microchannel for all the flow patterns generated in the three solvent pairs at org/aq (v/v) of (a) 0.25, (b) 1, and (c) 2.
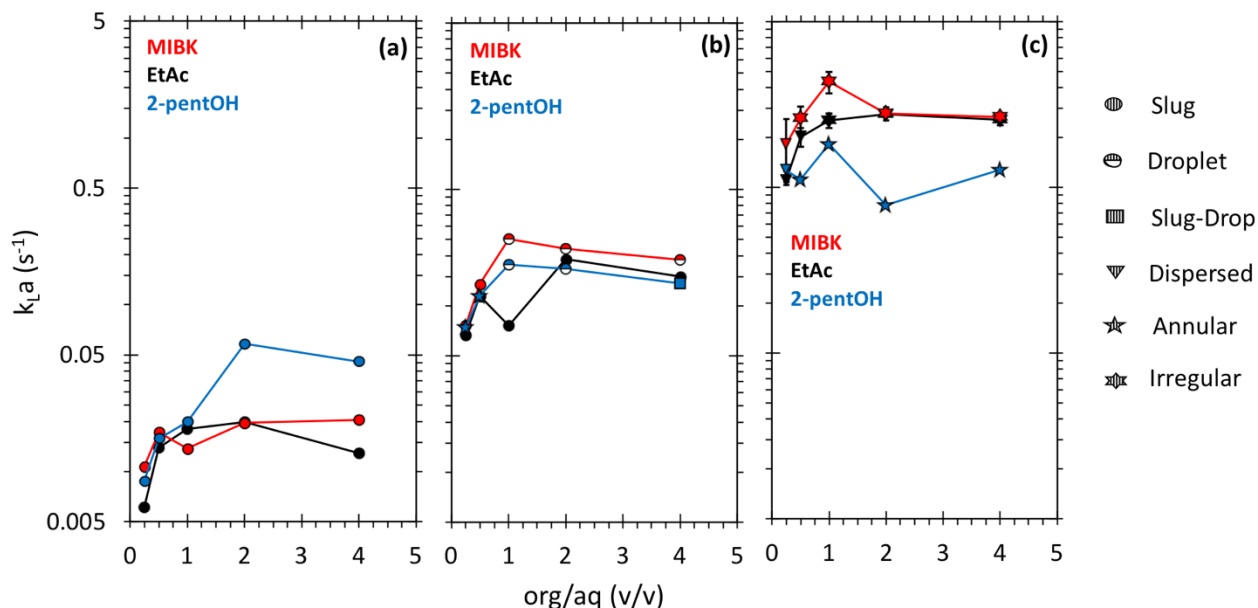
Figure 2. Effects of the org/aq (v/v) ratio on the volumetric mass transfer coefficient k_La obtained from experiments for three solvents at a fixed flow rate of (a) 0.1 mL/min, (b) 1 mL/min (b), and (c) 10 mL/min.

Model assessment

We assessed the numerical model by carrying out a direct comparison with the experiments in the same configuration. The experimental and numerical data in this section is obtained using a short 2 cm microchannel to reduce computational cost, compared to the 17 cm microchannel used in the previous section. The physical properties applied in CFD are shown in Table 1, and the diffusivity of HMF in the organic solvents is calculated using the Wilke-Chang correlation [53]. A wide range of total volumetric flow rates between 0.1 to 3 mL/min at unitary flow rate ratio are investigated, including the flow patterns of slug, droplet, parallel, and annular. Good agreement of flow patterns between simulations and experiments has been previously demonstrated [25]. Aside from the fluid dynamics, the C-CST approach has also been shown to have good performance for simulating interfacial mass transfer in the microchannel [50]. Moreover, Figure 3 compares the CFD-computed k_La to the experimental values, computed using Eq. (26), for three different solvent pairs. The simulations are in good agreement with the experiments for a wide range of k_La with relative deviations at most of 23%. The MIBK/water at 2.0 mL/min shows larger deviation, resulting from the difference in the flow patterns. Indeed, while parallel flow occurs in the experiment (Figure S2b(v)), droplet flow is observed in the simulation. This is attributed to the deviation of the interfacial tension estimation between the two phases in the VOF model [25]. The additional inner circulations of the droplet flow lead to increased mass transfer compared to the parallel flow. Overall, the computational model is generally accurate for all conditions, enabling the investigation of the transport mechanism.
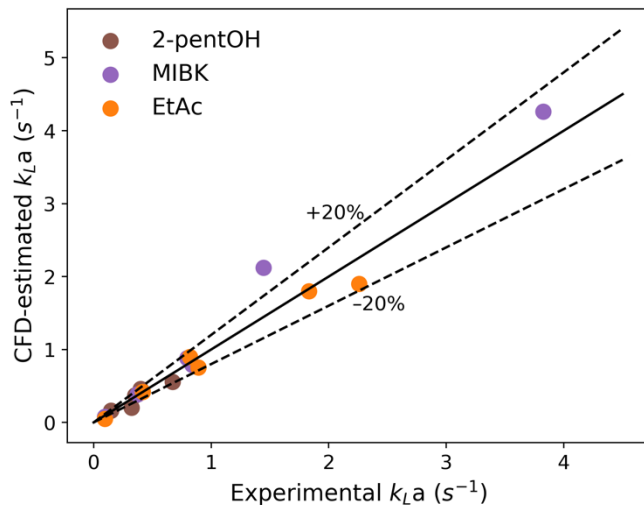
12

Figure 3. Parity plot for experimental and CFD-estimated overall mass transfer coefficient for three solvents at a total flow rate of 0.1–3 mL/min and org/aq (v/v) =1.

Transport mechanism in different flow regimes

To further understand the transport mechanism in different flow regimes, the concentration field (heatmap) and corresponding relative velocity field (arrows) at the middle of downstream microchannel are superimposed in Figure 4 for slug, droplet, and annular flow. The aqueous interface's position is highlighted with the isocontour at 0.9 of the water volume fraction. Three distinct flows are considered to discern the effect of the flow pattern on the mass transfer. Figure 4a presents the slug flow pattern, where inner circulations within both the aqueous and the organic slug are clearly observed. There are four vortexes within the aqueous slug, two longer ones, and two smaller ones at the front of the slug. The HMF concentration is much lower in the latter two small vortexes, indicating enhanced mass transfer across the interface at those regions, promoted by the inner circulations. The HMF concentration inside the two long vortexes is high. Moreover, the HMF concentration is much lower in the middle of the aqueous slug, compared to that inside the two long vortexes, indicating that mass transfer is mainly driven by advection in the axial direction, in agreement with the larger relative velocity in the middle of the slug. Aside from axial mass transfer, mass transport also slowly occurs in the radial direction, driven by diffusion and inner circulations. Figure 4b shows similar phenomena in the droplet flow of fast mass transfer in the middle of the slug in the axial direction and slow mass transfer in the radial direction. Interestingly, instead of similar HMF concentration at the top and bottom vortexes inside the aqueous slug, the HMF concentration is higher in the bottom vortexes of the aqueous droplet. The higher HMF concentration promotes the mass transfer in the lower part of the channel and particularly in the droplet's tail. This is attributed to the formation mechanism of droplet flow. The fast shear-off happens at some distance from the T-junction to form a droplet [66, 67], resulting in a short mixing time inside the aqueous droplet. Figure 4c highlights no inner circulations in the annular flow. Since the aqueous and organic phases flow in parallel, the mass transfer, driven by radial diffusion, is much slower. This fact explains the lower extraction efficiency for annular and parallel flow observed in the experiments.
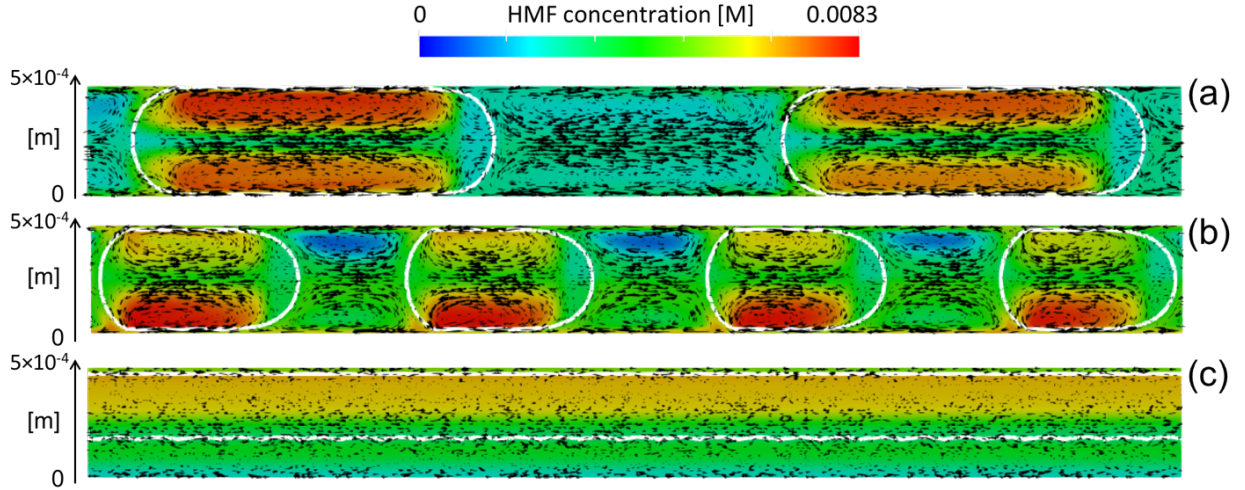
13

Figure 4. Predicted HMF concentration profile (heatmap) and relative velocity field (arrows) for (a) slug flow (0.2 mL/min; org/aq (v/v) = 1), (b) droplet flow (1 mL/min; org/aq (v/v) = 1), and (c) annular flow (5 mL/min; org/aq (v/v) = 1) of the EtAc/water. The white line represents the shape of the aqueous flow pattern.

Deconvolution of convective and diffusive contributions to transport

Since both convection and diffusion contribute to the interfacial mass transfer, it is important to deconvolute their contribution. In this regard, we first apply the surface renewal theory to calculate the individual mass transfer coefficient $k_{L,i}$ of each phase. The surface renewal theory is an extension of the penetration theory and considers that the liquid elements at the interface randomly exchange fresh elements with the bulk [68]. The surface renewal theory expresses the individual mass transfer coefficient as the square root of diffusion coefficient times the surface renewal rate [48], as shown in Eq. (26),

$$k_{L,i} = \sqrt{D_{j,i}s} \tag{26}$$

where *s* is the surface renewal rate estimated as the inverse residence time of the liquid and *i* identifies the phase. Upon computing the individual mass transfer coefficients in the aqueous and organic phases, we estimate the global mass transfer coefficient k_L for interfacial mass transfer from the resistance in each phase, assuming the mass transfer rates at steady state are equal[65]:

$$k_L = \frac{1}{\frac{K}{k_{L,1}} + \frac{1}{k_{L,2}}} \tag{27}$$

k_L is then multiplied by the specific surface area to obtain the theoretical $k_L a$ and is compared with the CFD-estimated value. To assess the predicted accuracy of the theoretical $k_L a$, we simulate the parallel flow, where mass transfer is driven by diffusive transport alone, at a residence time of 0.1 s for three organic solvents (EtAc, MIBK, and 2-pentOH) and additional cases using hypothetical diffusivities in a range from 10^{-10} to 10^{-8} m^2/s with the same density, viscosity, and interfacial tension as EtAc. Figure 5 shows that the theoretical $k_L a$ is in good agreement with the CFD-estimated value for a wide range of diffusivities within 10% error, indicating that it is adequate to use the surface renewal theory to approximate the diffusive mass transfer across the

14

interface. k_La in the 2-pentOH/water is the lowest among the three investigated organic solvents. Since the specific surface area of parallel flow of all three organic solvents is the same, the k_L of the 2-pentOH/water solvent-pair is the lowest. This is attributed to the lowest diffusivity of HMF therein.
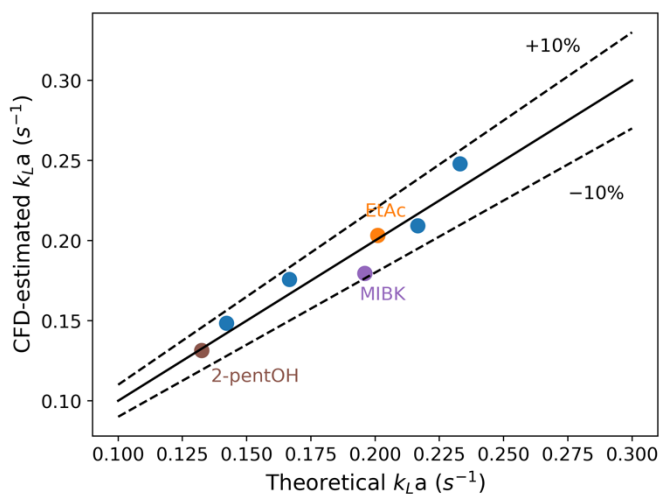

Figure 5. Parity plot for theoretical and CFD-estimated overall mass transfer coefficient. Full circles in blue are predictions using hypothetical diffusivities, with other properties being those of EtAc.

To calculate the diffusion-driven k_La using surface renewal theory, we first estimate the specific surface area of slug and droplet flow and consider the water/EtAc solvent-pair as an example. First, the specific surface area is calculated using the surface area and the volume of the slug and droplet obtained from the CFD simulations. Specifically, these properties are evaluated from the isocontour at 0.9 of water volume fraction to isolate the slug and droplet using the Paraview post-processing tool. Figure 6a shows that the specific surface area increases with increasing the total flow rate because the slug length decreases. Moreover, the specific surface area of the slug/droplet flow ($\sim 10^4$ m^2/m^3) is higher compared to that of the annular/parallel flow ($\sim 4 \times 10^3$ m^2/m^3) and demonstrates the micro-scale system's advantage of high specific surface area compared to a typical batch reactor. The diffusion-driven k_La_d is calculated using the theoretical k_L and the specific surface area. The convection-driven k_La_c is finally obtained by subtracting the diffusion-driven k_La from the overall k_La. In this way, the contributions of diffusion and convection are deconvoluted. In Figure 6b, both k_La_d and k_La_c increase when the total flow rate increases. k_La_c increases more than k_La_d, indicating that total flow rate affects more convective transport. The increase in k_La_d by the change of the total flow rate is mostly attributed to the increase of specific surface area due to the smaller slugs and droplets. The diffusive and convective contribution to transport (Figure 6c) shows that the latter gains from 30 to 55% when the total flow rate changes from 0.2 to 2.0 mL/min, indicating convection dominance at high flow rates. In contrast, the interfacial mass transfer relies mostly on diffusion at low flow rates. A noticeable contribution from convection (30%), due to the axial inner circulations within slugs and droplets, still plays a vital role in the interfacial mass transfer under the diffusion-dominated conditions.

15

Therefore, aside from the diffusive transport, it is also essential to consider convective transport while designing the system.
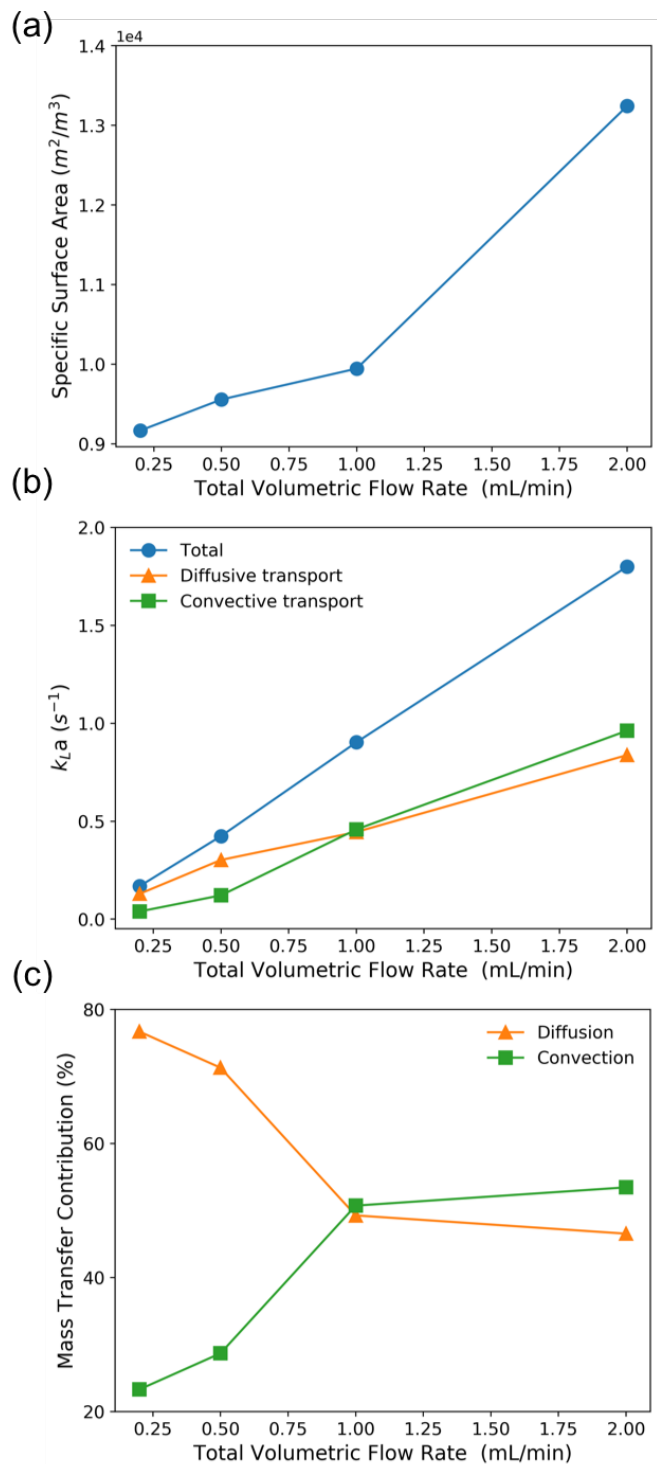

Figure 6. Predicted (a) specific surface areas, (b) various volumetric mass transfer coefficients, and (c) mass transfer contributions at different total volumetric flow rates of EtAc/water.

16

The extraction efficiency of biphasic systems

As mentioned earlier, the extraction efficiency is another important metric of the mass transfer process. Using the experimental measurements in Figure 1, Figure 7 plots the extraction efficiency vs. the total flow rate and the mean residence time for all the flow patterns at fixed org/aq (v/v) ratios. The flow conditions and flow patterns strongly influence the extraction efficiency. For all solvent pairs, at a fixed org/aq (v/v) ratio, the extraction efficiency varies non-monotonically with increasing total flow rate or decreasing mean residence time due to varying contributions of the mass transfer mechanism with changes in flow patterns. Moreover, the extraction efficiency delineates the optimal flow conditions for HMF extraction for each organic solvent.

Specifically, 2-pentOH usually provides a lower k_La (Figure 1) and a lower extraction efficiency at high flow rates (>1 mL/min), suggesting that this solvent is not adequate for high throughput (short contact times) HMF extraction. EtAc performs poorly at an org/aq (v/v) ratio of 1 with the lowest extraction efficiency during the transitions from slug flow to droplet flow and then to annular flow at a total flow rate ranging from 1 – 5 mL/min (Figure 7b). Moreover, the extraction efficiency of EtAc also becomes low when the flow pattern changes from slug flow to dispersed flow at a low org/aq (v/v) ratio (Figure 7a). Similarly, the lowest extraction efficiency for MIBK occurs in the same flow rate range as EtAc but at a lower org/aq (v/v) < 1 during the transition from slug flow to parallel flow and then to irregular flow (Figure 7a). This indicates that a higher org/aq (v/v) ratio ≥ 1 may be required for better extraction efficiency.
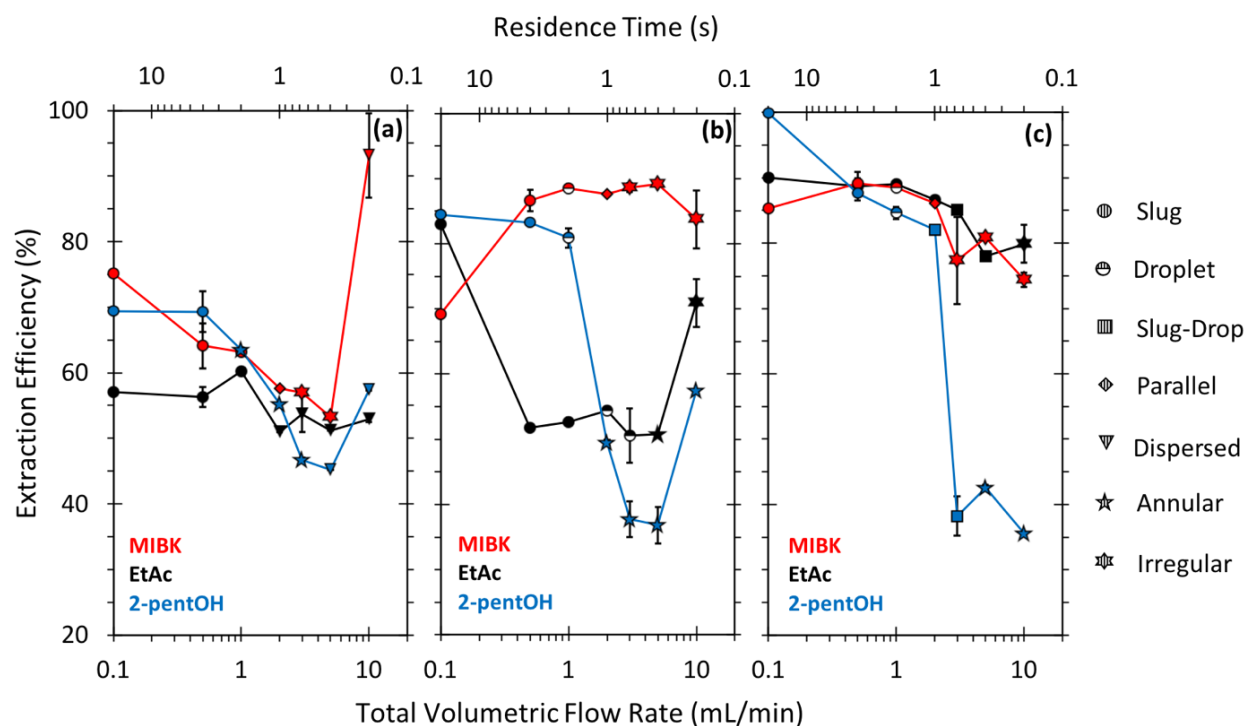

Figure 7. Percent extraction efficiency obtained from the experiments as a function of the total volumetric flow rate and the mean residence time in the microchannel for all flow patterns of three solvent pairs at org/aq (v/v) of (a) 0.25, (b) 1, and (c) 2.

17

Figure 8 shows the extraction efficiency vs. the org/aq (v/v) ratio at fixed flow rates for all three solvent pairs. The extraction efficiency is, in general, higher when the org/aq (v/v) ratio ≥ 1, but still varies non-monotonically as the org/aq (v/v) ratio increases at a given flow rate. As mentioned earlier, this is most likely due to changes in the dominant mass transport mechanism during the transition between flow regimes or within the same flow regime. Generally, a higher k_La leads to better extraction efficiency. At low and intermediate throughputs, the optimal conditions, determined for k_La of 2-pentOH and MIBK in Figure 1, also show the highest extraction efficiency as expected. Interestingly, at high throughput, MIBK/water irregular flow with org/aq (v/v) = 1 shows a higher k_La compared to EtAc/water irregular flow with org/aq (v/v) = 4 (2.17 s^{-1} vs. 1.33 s^{-1}), while the EtAc/water irregular flow with org/aq (v/v) = 4 shows slightly greater extraction efficiency than irregular flow with org/aq (v/v) = 1 (83.8% vs. 88.2%). Nonetheless, both the k_La and extraction efficiency are still comparable for both solvents. From a design perspective, flow regimes with org/aq (v/v) > 1 and extraction efficiencies >90% are ideal for HMF extraction. In Figure 8a, the 2-pentOH/water slug flow with org/aq (v/v) > 2 produces extraction efficiencies up to 99.9% in a low throughput (Q_{total} = 0.1 mL/min) microreactor. At intermediate throughput (Q_{total} = 1 mL/min), the MIBK/water droplet flow with org/aq (v/v) > 1 provides the best HMF extraction. For high throughput (Q_{total} = 10 mL/min), the EtAc/water irregular flow with org/aq (v/v) = 4 enables optimal extraction. These data show that high extraction efficiencies can be obtained under ultrashort residence times.
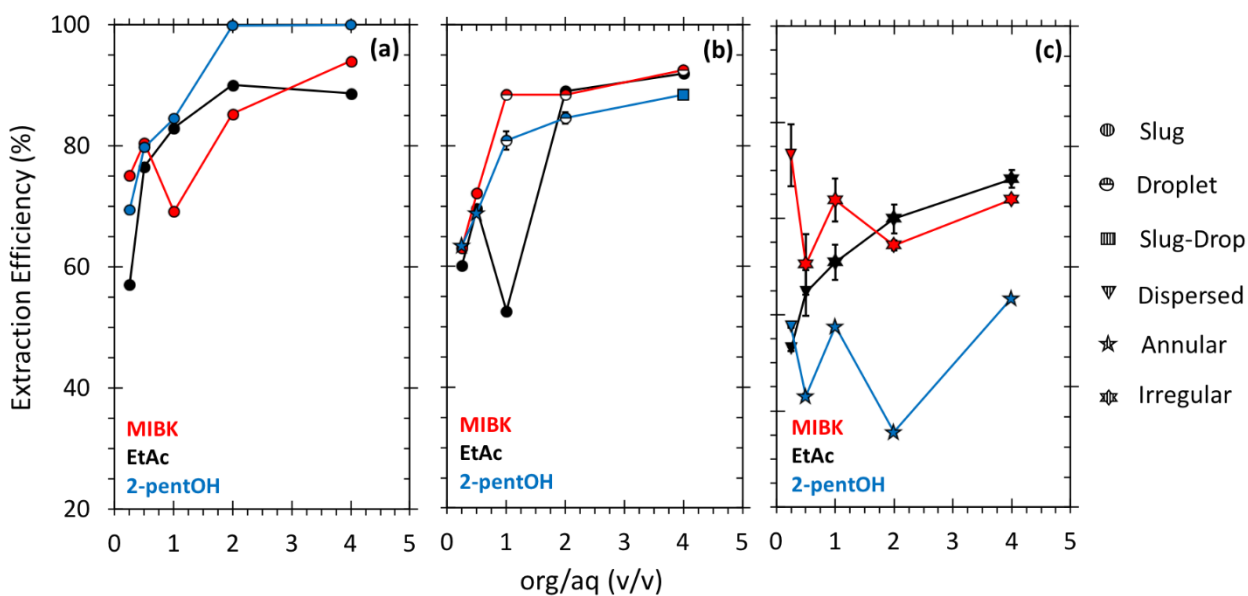

Figure 8. Influence of the org/aq (v/v) ratio on the percent extraction efficiency for three organic solvents at a fixed total flow rate of (a) 0.1 mL/min, (b) 1 mL/min, (c) 10 mL/min in the experiments.

Merit index

Our two-phase flow patterns show that biphasic microsystems can be effective for fast HMF extraction at high volumetric flow rates enabling higher throughput per reactor/extractor unit, reducing capital cost. Nonetheless, a higher pressure drop occurs at higher flow rates. Thereon, the energy expenditure due to pressure drop can potentially outweigh the enhancement in mass transfer rates and extraction efficiencies. From that perspective, we assessed the biphasic flow patterns by defining a dimensionless merit index (MI), which weights in the tradeoff between mass transfer and pressure drop. The MI is commonly used to compare flow reactors' performance using heterogeneous catalysts with foams and monolith reactors [69, 70]. The MI compares the mass transfer properties in terms of extraction efficiency with the dimensionless pressure drop

$$\text{MI} = -\frac{\ln(1-E)}{\left(\frac{\Delta P}{\rho_{mix}U^2}\right)} \tag{29}$$

$$\rho_{mix} = \varepsilon_{aq}\rho_{aq} + \varepsilon_{org}\rho_{org} \tag{30}$$

where ΔP is the pressure drop across the microchannel, ρ_{mix} is the biphasic mixture volume-averaged density, U is the biphasic mixture flow velocity, ρ_{aq} is the aqueous solvent density, and ρ_{org} is the organic solvent density. The higher the MI value, the better the tradeoff between mass transfer and pressure drop.

Figure 9a shows the pressure drop across the microchannel. For each biphasic system, the pressure losses increase by one order of magnitude as the total volumetric flow rate increases from 0.1 to 10 mL/min. Moreover, the 2-pentOH/water and EtAc/water biphasic flows produce the highest and lowest pressure drop, respectively, consistent with 2-pentOH having the highest kinematic viscosity and EtAc the lowest. Interestingly, the observed increase in pressure drop follows a quasi-linear trend with flow rate. Kashid and Agar[71] have also observed a similar linear increase of the pressure drop with increasing flow rates, using a cyclohexane/water slug flow generated in a Y-junction (ID = 500 μm) and a PTFE capillary channel (ID = 500 μm). They modeled the slug flow pressure drop by summing up two contributions: the hydrodynamic pressure drop (Hagen-Poiseulle) of the continuous phase (cyclohexane) and the pressure drop due to the organic film surrounding the aqueous slugs. They found reasonable agreement between the model predictions and the experimental pressure drop at org/aq (v/v) = 1. Thereon, in Figure 9a, at flow rates <1 mL/min in the slug flow regime, we understand that the pressure drop linearly increases with increasing flow rate based on the fact that both the hydrodynamic pressure drop of the organic phase and the pressure drop in the film region are directly proportional to the total flow rate. Moreover, at flow rates >1 mL/min, the slug flow transitions into regimes (droplet, annular, parallel, and irregular flow) where both shear and inertial forces dominate over capillary forces. In that case, the hydrodynamic pressure drop has a larger contribution to the pressure drop through the microchannel. The linear increase in pressure drop at higher flow rates is then a direct consequence of the linear dependence of the hydrodynamic pressure drop on the flow rate. Furthermore, Figure 9b plots the MI against the total flow rate. For each solvent pair, the MI value increases with increasing flow rates suggesting that at higher throughput, the improvement in mass transfer outweighs the penalty in pressure drop. Moreover, in the high flow rate range, the 2-pentOH/water flow patterns show the lowest MI values due to the lower extraction efficiency and higher pressure drop. MIBK/water and EtAc/water have comparable performance, reinforcing that

19

the latter biphasic mixture is optimal for effective HMF extraction under high throughput and fast flow conditions.
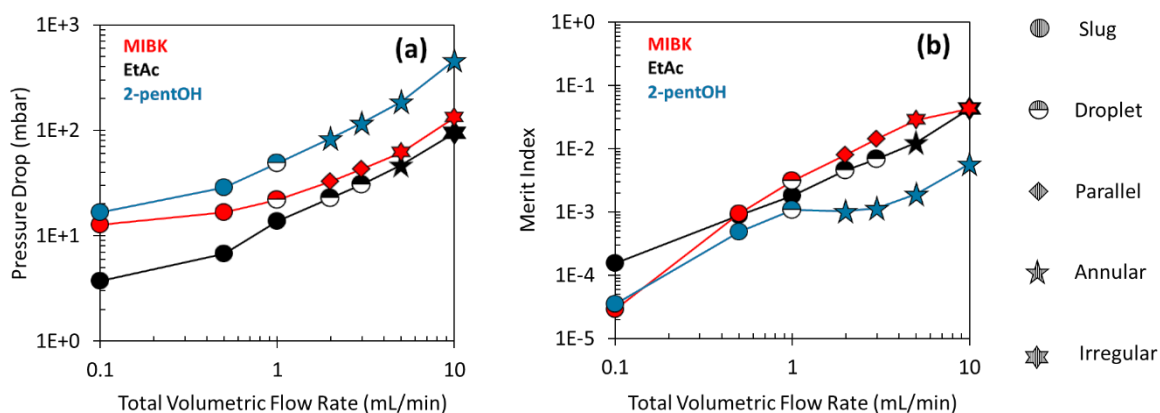

Figure 9. Effect of the total volumetric flow rate on the (a) pressure drop and the (b) merit index obtained from experiments for the three solvent pairs.

Conclusions

In this study, we evaluated the mass transfer and extraction of HMF in MIBK/water, EtAc/water, and 2-pentOH/water from the aqueous phase at ultrashort residence times from 0.2 – 20 s in a biphasic microchannel experimentally. Seven two-phase flow patterns were generated for flow rates ranging from 0.1 to 10 mL/min: slug, droplet, slug-droplet, dispersed, parallel, annular, and irregular flow. The volumetric mass transfer coefficients range from 0.009 – 0.912 s^{-1}, 0.006 – 1.33 s^{-1}, and 0.016 – 2.17 s^{-1} using 2-pentOH, EtAc, and MIBK, respectively. The mass transfer coefficient generally increases with increasing total flow rate except for 2-pentOH, where the mass transfer coefficient varies non-monotonically due to the change of the underlying mass transport mechanism during the transition between flow regimes.

Furthermore, we developed a CFD model to describe fluid dynamics and interfacial mass transfer. The CFD simulation is in good quantitative agreement with the experiments. The model indicates that the dominant transport mechanism changes with changing flow patterns. The deconvolution of diffusion and convection contributions to mass transfer in slug and droplet flows indicates a dominant convective effect at high flow rates due to inner slug circulations.

Aside from the mass transfer coefficient, the extraction efficiency for different organic solvents was also studied. The 2-pentOH/water slug flow produces high extraction efficiencies up to 99.9% at low flow rates. The MIBK/water droplet flow and the EtAc/water irregular flow show extraction efficiencies >90% at intermediate and high reactor throughput. For these solvents, the volumetric mass transfer coefficient increases with increasing flow rate. In contrast, the mass transfer coefficient in the 2-pentOH/water system varies non-monotonically, as the flow pattern changes from droplet or slug-droplet flow to annular flow. A merit index was defined to account for the tradeoff between mass transfer and pressure drop. Significant enhancement in the mass transfer at high flow rates overweighs the pressure drop penalty. The EtAc/water irregular flow is optimal as

20

it balances high extraction efficiency, large volumetric mass transfer coefficient, and low-pressure drop.

In general, each solvent pair considered in this study can increase the mass transfer rate up to 2 orders of magnitude by changing the flow rate and flow rate ratio, enabling precise control of mass transfer-controlled vs. reaction kinetics-controlled regimes. Due to this tunability, microsystems can elucidate organic solvent effects on aqueous-phase reactions. Developing robust multiphase microreactor design principles for ultrafast reactive extraction is an important future task.

Conflicts of interest
There are no conflicts to declare.

Supporting information
Evaluation of mass transfer in the sampling zone; derivations of the standard continuous species transfer method; numerical mesh convergence analysis; experimental liquid-liquid flow patterns.

References
1.   Jahnisch, K.; Hessel, V.; Lowe, H.; Baerns, M., Chemistry in microstructured reactors. *Angewandte Chemie-International Edition* **2004,** 43, (4), 406-446.
2.   Mason, B. P.; Price, K. E.; Steinbacher, J. L.; Bogdan, A. R.; McQuade, D. T., Greener approaches to organic synthesis using microreactor technology. *Chemical Reviews* **2007,** 107, (6), 2300-2318.
3.   Chen, T.-Y.; Baker-Fales, M.; Vlachos, D. G., Operation and Optimization of Microwave-Heated Continuous-Flow Microfluidics. *Industrial & Engineering Chemistry Research* **2020,** 59, (22), 10418-10427.
4.   Wang, K.; Li, L.; Xie, P.; Luo, G., Liquid–liquid microflow reaction engineering. *Reaction Chemistry & Engineering* **2017,** 2, (5), 611-627.
5.   Zhao, C. X.; Middelberg, A. P. J., Two-phase microfluidic flows. *Chemical Engineering Science* **2011,** 66, (7), 1394-1411.

21

6.   Hoffmann, M.; Schluter, M.; Rabiger, N., Experimental investigation of liquid-liquid mixing in T-shaped micro-mixers using mu-LIF and mu-PIV. *Chemical Engineering Science* **2006,** 61, (9), 2968-2976.

7.   Zhao, Y. C.; Chen, G. W.; Yuan, Q., Liquid-liquid two-phase flow patterns in a rectangular microchannel. *Aiche Journal* **2006,** 52, (12), 4052-4060.

8.   Hartman, R. L., Flow chemistry remains an opportunity for chemists and chemical engineers. *Current Opinion in Chemical Engineering* **2020,** 29, 42-50.

9.   Zhang, J.; Wang, K.; Teixeira, A. R.; Jensen, K. F.; Luo, G., Design and Scaling Up of Microchemical Systems: A Review. *Annual Review of Chemical and Biomolecular Engineering* **2017,** 8, (1), 285-305.

10.   Kashid, M. N.; Harshe, Y. M.; Agar, D. W., Liquid-liquid slug flow in a capillary: An alternative to suspended drop or film contactors. *Industrial & Engineering Chemistry Research* **2007,** 46, (25), 8420-8430.

11.   Tsaoulidis, D.; Angeli, P., Effect of channel size on mass transfer during liquid-liquid plug flow in small scale extractors. *Chemical Engineering Journal* **2015,** 262, 785-793.

12.   Woitalka, A.; Kuhn, S.; Jensen, K. F., Scalability of mass transfer in liquid-liquid flow. *Chemical Engineering Science* **2014,** 116, 1-8.

13.   Li, G.; Pu, X.; Shang, M.; Zha, L.; Su, Y., Intensification of liquid–liquid two-phase mass transfer in a capillary microreactor system. *AIChE Journal* **2019,** 65, (1), 334-346.

14.   Wang, K.; Luo, G., Microflow extraction: A review of recent development. *Chemical Engineering Science* **2017,** 169, 18-33.

15.   Sattari-Najafabadi, M.; Nasr Esfahany, M.; Wu, Z.; Sundén, B., Hydrodynamics and mass transfer in liquid-liquid non-circular microchannels: Comparison of two aspect ratios and three junction structures. *Chemical Engineering Journal* **2017,** 322, 328-338.

16.   Jovanovic, J.; Rebrov, E. V.; Nijhuis, T. A.; Kreutzer, M. T.; Hessel, V.; Schouten, J. C., Liquid-Liquid Flow in a Capillary Microreactor: Hydrodynamic Flow Patterns and Extraction Performance. *Industrial & Engineering Chemistry Research* **2012,** 51, (2), 1015-1026.

17.   Assmann, N.; Ladosz, A.; von Rohr, P. R., Continuous Micro Liquid-Liquid Extraction. *Chemical Engineering & Technology* **2013,** 36, (6), 921-936.

18.   Anna, S. L.; Bontoux, N.; Stone, H. A., Formation of dispersions using "flow focusing" in microchannels. *Applied Physics Letters* **2003,** 82, (3), 364-366.

19.   Christopher, G. F.; Anna, S. L., Microfluidic methods for generating continuous droplet streams. *Journal of Physics D-Applied Physics* **2007,** 40, (19), R319-R336.

20.   Gunther, A.; Jensen, K. F., Multiphase microfluidics: from flow characteristics to chemical and materials synthesis (vol 6, pg 1487, 2006). *Lab on a Chip* **2007,** 7, (3), 399-399.

21.   Dessimoz, A. L.; Cavin, L.; Renken, A.; Kiwi-Minsker, L., Liquid-liquid two-phase flow patterns and mass transfer characteristics in rectangular glass microreactors. *Chemical Engineering Science* **2008,** 63, (16), 4035-4044.

22.   Kashid, M. N.; Agar, D. W., Hydrodynamics of liquid–liquid slug flow capillary microreactor: Flow regimes, slug size and pressure drop. *Chemical Engineering Journal* **2007,** 131, (1), 1-13.

23.   Kashid, M. N.; Renken, A.; Kiwi-Minsker, L., Influence of Flow Regime on Mass Transfer in Different Types of Microchannels. *Industrial & Engineering Chemistry Research* **2011,** 50, (11), 6906-6914.

24.   Dreyfus, R.; Tabeling, P.; Willaime, H., Ordered and disordered patterns in two-phase flows in microchannels. *Physical Review Letters* **2003,** 90, (14).

22

25.   Desir, P.; Chen, T.-Y.; Bracconi, M.; Saha, B.; Maestri, M.; Vlachos, D. G., Experiments and computations of microfluidic liquid–liquid flow patterns. *Reaction Chemistry & Engineering* **2020,** 5, (1), 39-50.

26.   Asghari, F. S.; Yoshida, H., Acid-catalyzed production of 5-hydroxymethyl furfural from D-fructose in subcritical water. *Industrial & Engineering Chemistry Research* **2006,** 45, (7), 2163-2173.

27.   Chheda, J. N.; Roman-Leshkov, Y.; Dumesic, J. A., Production of 5-hydroxymethylfurfural and furfural by dehydration of biomass-derived mono- and poly-saccharides. *Green Chemistry* **2007,** 9, (4), 342-350.

28.   Desir, P.; Saha, B.; Vlachos, D. G., Ultrafast flow chemistry for the acid-catalyzed conversion of fructose. *Energy & Environmental Science* **2019,** 12, (8).

29.   Chen, T.-Y.; Cheng, Z.; Desir, P.; Saha, B.; Vlachos, D. G., Fast microflow kinetics and acid catalyst deactivation in glucose conversion to 5-hydroxymethylfurfural. *Reaction Chemistry & Engineering* **2021,** 6, (1), 152-164.

30.   Tsilomelekis, G.; Orella, M. J.; Lin, Z. X.; Cheng, Z. W.; Zheng, W. Q.; Nikolakis, V.; Vlachos, D. G., Molecular structure, morphology and growth mechanisms and rates of 5-hydroxymethyl furfural (HMF) derived humins. *Green Chemistry* **2016,** 18, (7), 1983-1993.

31.   Girisuta, B.; Janssen, L.; Heeres, H. J., A kinetic study on the decomposition of 5-hydroxymethylfurfural into levulinic acid. *Green Chemistry* **2006,** 8, (8), 701-709.

32.   Cheng, Z.; Everhart, J. L.; Tsilomelekis, G.; Nikolakis, V.; Saha, B.; Vlachos, D. G., Structural analysis of humins formed in the Brønsted acid catalyzed dehydration of fructose. *Green Chemistry* **2018,** 20, (5), 997-1006.

33.   Nikolla, E.; Roman-Leshkov, Y.; Moliner, M.; Davis, M. E., "One-Pot" Synthesis of 5-(Hydroxymethyl)furfural from Carbohydrates using Tin-Beta Zeolite. *Acs Catalysis* **2011,** 1, (4), 408-410.

34.   Pagan-Torres, Y. J.; Wang, T. F.; Gallo, J. M. R.; Shanks, B. H.; Dumesic, J. A., Production of 5-Hydroxymethylfurfural from Glucose Using a Combination of Lewis and Bronsted Acid Catalysts in Water in a Biphasic Reactor with an Alkylphenol Solvent. *Acs Catalysis* **2012,** 2, (6), 930-934.

35.   Roman-Leshkov, Y.; Dumesic, J. A., Solvent Effects on Fructose Dehydration to 5-Hydroxymethylfurfural in Biphasic Systems Saturated with Inorganic Salts. *Topics in Catalysis* **2009,** 52, (3), 297-303.

36.   Saha, B.; Abu-Omar, M. M., Advances in 5-hydroxymethylfurfural production from biomass in biphasic solvents. *Green Chemistry* **2014,** 16, (1), 24-38.

37.   Shimanouchi, T.; Kataoka, Y.; Tanifuji, T.; Kimura, Y.; Fujioka, S.; Terasaka, K., Chemical Conversion and Liquid-Liquid Extraction of 5-Hydroxymethylfurfural from Fructose by Slug Flow Microreactor. *Aiche Journal* **2016,** 62, (6), 2135-2143.

38.   Desir, P.; Saha, B.; Vlachos, D. G., Ultrafast flow chemistry for the acid-catalyzed conversion of fructose. *Energy & Environmental Science* **2019,** 12, (8), 2463-2475.

39.   Lueckgen, J.; Vanoye, L.; Philippe, R.; Eternot, M.; Fongarland, P.; de Bellefon, C.; Favre-Reguillon, A., Simple and selective conversion of fructose into HMF using extractive-reaction process in microreactor. *Journal of Flow Chemistry* **2018,** 8, (1), 3-9.

40.   Muranaka, Y.; Nakagawa, H.; Masaki, R.; Maki, T.; Mae, K., Continuous 5-Hydroxymethylfurfural Production from Monosaccharides in a Microreactor. *Industrial & Engineering Chemistry Research* **2017,** 56, (39), 10998-11005.

41. Tuercke, T.; Panic, S.; Loebbecke, S., Microreactor Process for the Optimized Synthesis of 5-Hydroxymethylfurfural: A Promising Building Block Obtained by Catalytic Dehydration of Fructose. *Chemical Engineering & Technology* **2009,** 32, (11), 1815-1822.

42. Zhou, C. J.; Shen, C.; Ji, K. Y.; Yin, J. B.; Du, L., Efficient Production of 5-Hydroxymethylfurfural Enhanced by Liquid-Liquid Extraction in a Membrane Dispersion Microreactor. *Acs Sustainable Chemistry & Engineering* **2018,** 6, (3), 3992-+.

43. Brasholz, M.; von Känel, K.; Hornung, C. H.; Saubern, S.; Tsanaktsidis, J., Highly efficient dehydration of carbohydrates to 5-(chloromethyl)furfural (CMF), 5-(hydroxymethyl)furfural (HMF) and levulinic acid by biphasic continuous flow processing. *Green Chemistry* **2011,** 13, (5), 1114-1117.

44. Haroun, Y.; Legendre, D.; Raynal, L., Volume of fluid method for interfacial reactive mass transfer: Application to stable liquid film. *Chemical Engineering Science* **2010,** 65, (10), 2896-2909.

45. Marschall, H.; Hinterberger, K.; Schüler, C.; Habla, F.; Hinrichsen, O., Numerical simulation of species transfer across fluid interfaces in free-surface flows using OpenFOAM. *Chemical Engineering Science* **2012,** 78, 111-127.

46. Deising, D.; Marschall, H.; Bothe, D., A unified single-field model framework for Volume-Of-Fluid simulations of interfacial species transfer applied to bubbly flows. *Chemical Engineering Science* **2016,** 139, 173-195.

47. Falcone, M.; Bothe, D.; Marschall, H., 3D direct numerical simulations of reactive mass transfer from deformable single bubbles: An analysis of mass transfer coefficients and reaction selectivities. *Chemical Engineering Science* **2018,** 177, 523-536.

48. Nieves-Remacha, M. J.; Yang, L.; Jensen, K. F., OpenFOAM Computational Fluid Dynamic Simulations of Two-Phase Flow and Mass Transfer in an Advanced-Flow Reactor. *Industrial & Engineering Chemistry Research* **2015,** 54, (26), 6649-6659.

49. Yang, L.; Nieves-Remacha, M. J.; Jensen, K. F., Simulations and analysis of multiphase transport and reaction in segmented flow microreactors. *Chemical Engineering Science* **2017,** 169, 106-116.

50. Maes, J.; Soulaine, C., A new compressive scheme to simulate species transfer across fluid interfaces using the Volume-Of-Fluid method. *Chemical Engineering Science* **2018,** 190, 405-418.

51. Maes, J.; Soulaine, C., A unified single-field Volume-of-Fluid-based formulation for multi-component interfacial transfer with local volume changes. *Journal of Computational Physics* **2020,** 402, 109024.

52. Zhao, Y.; Chen, G.; Yuan, Q., Liquid-liquid two-phase mass transfer in the T-Junction microchannels. *AIChE Journal* **2007,** 53, 3042-3053.

53. Wilke, C. R.; Chang, P., Correlation of diffusion coefficients in dilute solutions. *AIChE Journal* **1955,** 1, (2), 264-270.

54. Gueyffier, D.; Li, J.; Nadim, A.; Scardovelli, R.; Zaleski, S., Volume-of-fluid interface tracking with smoothed surface stress methods for three-dimensional flows. *Journal of Computational Physics* **1999,** 152, (2), 423-456.

55. Hirt, C. W.; Nichols, B. D., VOLUME OF FLUID (VOF) METHOD FOR THE DYNAMICS OF FREE BOUNDARIES. *Journal of Computational Physics* **1981,** 39, (1), 201-225.

56. Rusche, H. Computational fluid dynamics of dispersed two-phase flows at high phase fractions. University of London, 2002.

57.   Berberovic, E.; van Hinsberg, N. P.; Jakirlic, S.; Roisman, I. V.; Tropea, C., Drop impact onto a liquid layer of finite thickness: Dynamics of the cavity evolution. *Physical Review E* **2009,** 79, (3).

58.   Brackbill, J. U.; Kothe, D. B.; Zemach, C., A continuum method for modeling surface tension. *Journal of Computational Physics* **1992,** 100, (2), 335-354.

59.   Scardovelli, R.; Zaleski, S., DIRECT NUMERICAL SIMULATION OF FREE-SURFACE AND INTERFACIAL FLOW. *Annual Review of Fluid Mechanics* **1999,** 31, (1), 567-603.

60.   Raeini, A. Q.; Blunt, M. J.; Bijeljic, B., Direct simulations of two-phase flow on micro-CT images of porous media and upscaling of pore-scale forces. *Advances in Water Resources* **2014,** 74, 116-126.

61.   Francois, M. M.; Cummins, S. J.; Dendy, E. D.; Kothe, D. B.; Sicilian, J. M.; Williams, M. W., A balanced-force algorithm for continuous and sharp interfacial surface tension models within a volume tracking framework. *Journal of Computational Physics* **2006,** 213, (1), 141-173.

62.   Hoang, D. A.; van Steijn, V.; Portela, L. M.; Kreutzer, M. T.; Kleijn, C. R., Benchmark numerical simulations of segmented two-phase flows in microchannels using the Volume of Fluid method. *Computers & Fluids* **2013,** 86, 28-36.

63.   Graveleau, M.; Soulaine, C.; Tchelepi, H. A., Pore-Scale Simulation of Interphase Multicomponent Mass Transfer for Subsurface Flow. *Transport in Porous Media* **2017,** 120, (2), 287-308.

64.   Weller, H. G.; Tabor, G.; Jasak, H.; Fureby, C., A tensorial approach to computational continuum mechanics using object-oriented techniques. *Computers in Physics* **1998,** 12, (6), 620-631.

65.   Kashid, M. N.; Renken, A.; Kiwi-Minsker, L., Gas–liquid and liquid–liquid mass transfer in microstructured reactors. *Chemical Engineering Science* **2011,** 66, (17), 3876-3897.

66.   De Menech, M.; Garstecki, P.; Jousse, F.; Stone, H. A., Transition from squeezing to dripping in a microfluidic T-shaped junction. *Journal of Fluid Mechanics* **2008,** 595, 141-161.

67.   Garstecki, P.; Fuerstman, M. J.; Stone, H. A.; Whitesides, G. M., Formation of droplets and bubbles in a microfluidic T-junction—scaling and mechanism of break-up. *Lab on a Chip* **2006,** 6, (3), 437-446.

68.   Danckwerts, P. V., Significance of Liquid-Film Coefficients in Gas Absorption. *Industrial & Engineering Chemistry* **1951,** 43, (6), 1460-1467.

69.   Giani, L.; Groppi, G.; Tronconi, E., Mass-Transfer Characterization of Metallic Foams as Supports for Structured Catalysts. *Industrial & Engineering Chemistry Research* **2005,** 44, (14), 4993-5002.

70.   Bracconi, M.; Ambrosetti, M.; Okafor, O.; Sans, V.; Zhang, X.; Ou, X.; Da Fonte, C. P.; Fan, X.; Maestri, M.; Groppi, G.; Tronconi, E., Investigation of pressure drop in 3D replicated open-cell foams: Coupling CFD with experimental data on additively manufactured foams. *Chemical Engineering Journal* **2019,** 377, 120123.

71.   Kashid, M. N.; Agar, D. W., Hydrodynamics of liquid-liquid slug flow capillary microreactor: Flow regimes, slug size and pressure drop. *Chemical Engineering Journal* **2007,** 131, (1-3), 1-13.

25

Table of contents